# Strain Accumulation in Polymer Electrolyte Membrane and Membrane Electrode Assembly Materials During a Single Hydration/Dehydration Cycle

**Louis G. Hector, Jr.**
Materials and Processes Lab,
General Motors R & D Center,
Warren, MI 48090-9055

**Yeh-Hung Lai**
GM Fuel Cell Activities,
Honeoye Falls, NY 14472-0603

**Wei Tong**
Department of Mechanical Engineering,
Southern Methodist University,
Dallas, TX 75275-0337

**Michael J. Lukitsch**
Materials and Processes Lab,
General Motors R & D Center,
Warren, MI 48090-9055

*A digital image correlation technique was used to measure drying-induced strains in perfluorosulfonic acid (PFSA) membrane and membrane electrode assembly (MEA) materials which are key components of fuel cells. Circular coupons of each material were constrained in a stainless-steel drum fixture and hydration was achieved by immersing the drum/coupon assembly in $80°C$ water for 5 min. During air drying at $25°C$ and 50% relative humidity, a series of $1280 \times 960$ digital images of each coupon surface was recorded with a digital camera and image acquisition system for drying periods up to 26 h. Cumulative correlation of an initial image recorded prior to hot water immersion and the final image at the end of drying produced in-plane strain contour maps. Incremental correlation was employed to track strain evolution at the coupon centers and at peripheral points. During the earliest drying stages, where both materials exhibited viscoelastic behavior, peak radial strains of 9.50% and 2.50% were measured in the PFSA membrane and MEA materials, respectively. At longer drying times, peak radial strains reached constant values of 5.70% and 1.25% in the PFSA membrane and MEA materials, respectively. Strain accumulation in the MEA tends to be less uniform than that in the membrane, and corresponding peak strain values in the MEA tend to be less than those in the membrane independent of drying duration. Reinforcement from the electrode layers lowers strain accumulation in the MEA, but it does not preclude crack nucleation in these layers as drying proceeds.* [DOI: 10.1115/1.2393302]

## 1 Introduction

Membrane electrode assemblies (MEAs), composed of a polymer electrolyte membrane (PEM) sandwiched between two catalyst-loaded electrode layers, are integral components of automotive fuel cells. [1]. The PEM conducts protons from the anode electrode to the cathode electrode of the fuel cell while preventing crossover of the reactant gases, $H_2$ and $O_2$. State-of-the-art PEM fuel cells utilize perfluorosulfonic acid (PFSA) membranes that are typically no more than 50 $\mu$m thick. Fuel cells cannot operate effectively if small amounts of gas are able to permeate the membrane through microscopic cracks which are commonly referred to as pinholes. Many premature failures in PEM fuel cells are attributed to pinhole nucleation within the polymer membranes (due to mechanical stresses [2]) which diminishes proton conductivity due to increased cross-over leaks of $H_2$ gas. It is therefore critical that all membranes in a fuel cell stack be mechanically durable against in-service stresses.

Among the different stresses induced under various fuel cell operating conditions, those due to shrinkage, leading to shrink tension [2,3], are of great interest since shrinkage contributes to pinhole nucleation. As the fuel cell undergoes operation cycles, the membrane goes through cycles of shrink tension and stress relaxation, which effectively amount to fatigue cycles. Experimental measurement of drying-induced strains in membrane materials is quite challenging since it is important not to disturb the drying process while measuring strains with a strain gauge (for example) which size and location are user controlled. Methods

such as Moiré [4] or Fizeau interferometry [5] are likely impractical due to sample preparation and/or complex experimental configurations.

Reported mechanical tests of membrane materials have largely focused on the thermal and mechanical properties of PFSA membranes using dynamic mechanical analysis and/or thermogravimetric analysis [6]. However, there is a dearth of published work on deformation measurement due to drying induced shrinkage. Although it is common to see reports on the water uptake and dimensional swelling of PFSA membranes, shrinkage data in the membrane is typically not mentioned. An exception is the recent work of Gittleman et al. [3], who measured dimensional changes of Nafion® membranes [7] in both the swollen and shrunk states. Rectangular Nafion® NR111 coupons were found to swell by 15% along their lengths and widths, and 26% in the thickness direction following immersion in water at $80°C$ (i.e., the normal fuel cell operating temperature) for 2.5 h. Upon drying to 3%RH at $80°C$, the length and width directions diminished by 3–4%. The thickness direction had a residual swelling of 0.5%. It was also reported that Nafion membranes exhibited a residual uniaxial shrink tension of 1.5 to 2.3 MPa at 30%RH, $25°C$.

In this paper, measurements of in-plane strain fields accumulated in PEM and MEA materials during a simulated hydration/dehydration cycle are presented. While it represents highly idealized conditions (e.g., normal fuel cell operation will involve many hydration/dehydration cycles), the single hydration/dehydration cycle was sufficient to generate strains that could be accurately quantified with digital image correlation (DIC). The remainder of the paper is organized as follows. Section 2 contains a discussion of the materials tested in this work and the experimental system. Representative in-plane strain contour patterns generated from
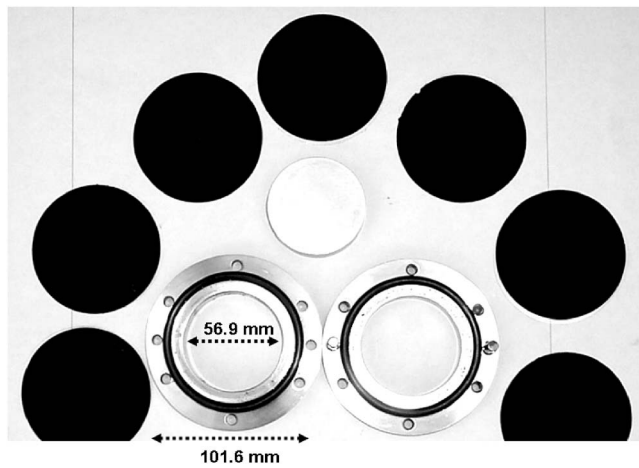
**Fig. 1  Sample MEA (black) coupons (75 mm diameter), disassembled stainless steel drum halves (top half on the left, bottom half on the right) with 56.9 and 101.6 mm inner and outer diameters, respectively, rubber seals (black rings just inside bolt circles) and mounting disk (center).**
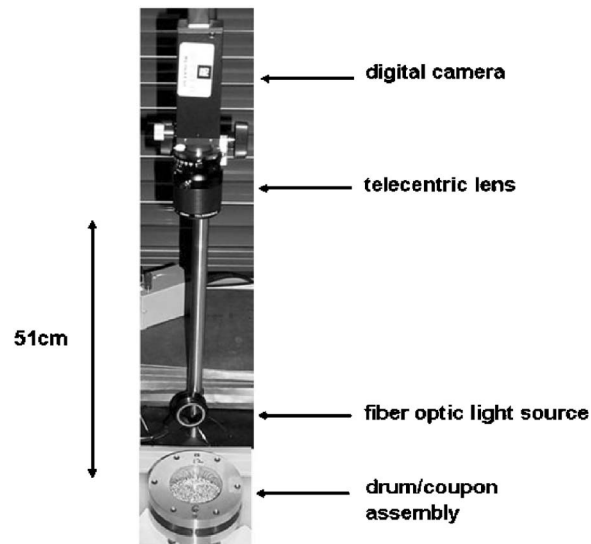


**Fig. 2  Experimental configuration showing digital camera with telecentric lens, fiber optic light source, and drum/coupon assembly. The light-diffusing curtain is not shown. The fiber optic light source is positioned for the top-illumination mode.**

digital images captured from the surfaces of the materials during air drying are discussed in Sec. 3. Also discussed are mechanical strain evolution during drying using incremental correlation at selected peripheral points, and changes in MEA crack density. The major results of this work are summarized in Sec. 4.

## 2  Experimental Details

**2.1  Polymer Electrolyte Membrane.** An 18-$\mu$m-thick version of the micro-reinforced, composite expanded polytetrafluoroethylene (ePTFE, a form of Teflon® reinforcement) polymer electrolyte membrane was used. Detailed information about the membrane material employed in the present study may be found in [8]. The PFSA fluoroionomer is a modified PTFE with a sulfonated side chain [9]. The side chain is terminated with an $SO_3^-$ group that renders the membrane hydrophyllic and facilitates proton flow through the electrolyte membrane. The tensile modulus of elasticity ranges between 350 MPa when dry at 20°C, to 50 MPa at 80°C when fully hydrated using ASTM D882 [10]. Upon hydration at 80°C by submerging in water, an unconstrained membrane swells in the in-plane direction by 13–18% and then shrinks by 6–8% relative to its original dimensions upon drying. The thickness change is about 40–46% when hydrated, and about 3% upon drying. It should be noted that the dimensional stability behavior of PFSA membranes may vary depending on the prior history of the material before testing. All samples used in this study received no special treatment other than retention at laboratory conditions of 50%RH and 25°C.

**2.2  Membrane Electrode Assembly.** The membrane electrode assembly (MEA) consists of carbon-support catalyst material that is hot pressed onto both sides of a PFSA polymer membrane. The platinum catalyst is dispersed across the carbon support. Each electrode layer is 12 $\mu$m thick. Through-the-electrode-thickness cracks (referred to as "mud cracks") can be found on either side of the electrodes. The crack length is typically several times the electrode thickness. Pinholes are often found in the membrane at the base of the mud cracks [2]. Since mud cracks can serve as the location of stress concentrations, it is likely that they are associated with pinhole nucleation, and ultimately to MEA failure.

**2.3  Drum Fixture.** Sample MEA coupons, along with the stainless steel drum fixture halves, rubber seals, and mounting disk are shown in Fig. 1. Each 75-mm-diameter coupon was cut

using a precision die set and then placed in the drum fixture which consisted of two mating halves. The PFSA coupons (not shown in Fig. 1) were cut to the same size. Each half of the drum fixture was machined with a raised lip, the surfaces of which came into contact during assembly. The inner diameter of each drum half was 56.9 mm (which denotes the radial field of view of the coupon surface), and the outer diameter of each drum half was 101.6 mm. A rubber seal was placed along the outer circumference of each lip to facilitate coupon mounting and clamping. The diameter of each coupon was such that its outer circumference covered the exposed surface of each seal when the coupon was positioned with its center coinciding with the drum center. The bottom half of the drum assembly contained two guide pins for alignment. The drum fixture was held together with six screws. To eliminate wrinkling, a stainless steel mounting disk (with a 56 mm diameter) was placed underneath the coupon surface once it was set on the bottom drum half.

**2.4  Experimental Configuration.** Figure 2 shows the experimental configuration. The seven frames/s digital camera (SONY model XCD-SX900) had a 1280×960 pixel density. The camera, with an integral telecentric lens, was attached to a vertical pole (fixed to a horizontal base plate) and aligned along an axis directly above the center of the coupon surface with a 51 cm working distance. The telecentric lens minimized perspective distortion of the image and provided a field of view that included most of the coupon surface. Capture of the entire coupon surface was deemed unnecessary for display of the cumulative strain fields, which were computed over rectangular grids as mitigated by the DIC algorithm (which currently precludes direct strain measurement in polar coordinates). In addition, incremental mapping (for investigation of strain field evolution) required substantially smaller digital DIC grids than that shown in Fig. 3, localized at specific points of interest. Light from the fiber optic source was directed into a diffusing curtain (not shown in Fig. 2). Recorded image quality depended upon the camera f-stop (adjusted to allow the desired amount of light into the camera) and pixel density. Digital images captured with the camera/lens assembly were stored with a custom image acquisition algorithm based upon the DASYLab program [11].

**2.5  PFSA/MEA Coupon Preparation.** Prior to assembling the drum fixture, one surface of each coupon was decorated with
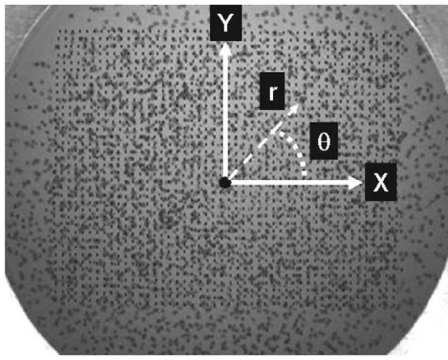
**Fig. 3 Schematic of polar coordinate system $(r, \theta)$ on a digital grid in a Cartesian $(X, Y)$ system superimposed on a PFSA membrane image. Solid circle represents $r=0$, $\theta=0$, i.e., center grid point in each coupon image.**

a high density of contrast features. What worked best for the PFSA membranes was an array of dots from a black (ultrafine point) indelible marker. Neither did the ink run, nor did it significantly fade during immersion and drying. A representative contrast pattern (irregular black dots behind digital grid points) is shown in Fig. 3. Note that the density of the dots did not need to be carefully controlled since image correlation identifies and tracks unique contrast features from image to image as deformation proceeds [12]. Digital images were recorded from that surface containing the contrast pattern under suitable illumination from the fiber optic light source in the so-called "top-illumination" mode shown in Fig. 2. For the MEA material, two contrast patterns were used. The first pattern was simply the light pattern resulting from illumination of overlapping mud cracks in both electrode layers. The fiber optic light source was placed underneath the drum/coupon assembly in Fig. 2 and suitably diffused so as to illuminate the entire MEA surface. Digital images were recorded from the surface on the side opposite of that which was illuminated. This "bottom-illumination" mode produced what we refer to as a "stars-at-night" pattern. The second contrast pattern was an array of white dots from an indelible marker (1.0 mm tip). Images were then recorded from the decorated MEA coupon surface that was illuminated in the "top illumination" mode. Note that the image exposure time (adjusted through the image acquisition software) was $1/32$ s for the membrane and bottom-illuminated MEA, and $1/8$ s for the MEA illuminated from the top.

**2.6 Digital Image Correlation.** After testing, DIC analyses of all PFSA membrane/MEA images were conducted with the SDMAP program detailed in [12]. The analysis involved either cumulative correlation, in which images recorded at much different times were correlated, or incremental correlation, in which temporally successive image pairs were correlated to capture the time evolution of drying-induced strains at specific points on the material surface. A digital grid pattern (which serves as a digital strain gauge) covering a rectangular area of each coupon surface, was computed and superimposed onto each image pair used for cumulative correlation (see Fig. 3). The position of the grid points as strains accumulated was contingent upon the DIC algorithm locating unique contrast features in the initial image and then tracking these features in all subsequent images during drying. The strains were then computed at each grid point once each test concluded. The spatial extent of the grid pattern and hence the region over which the calculation was conducted was user-controlled. Prior applications of the DIC technique are detailed in [13,14]. The reader is referred to [15–17] for detailed theoretical treatments.

A series of calibration tests was conducted prior to the

hydration/dehydration tests to evaluate the accuracy of the DIC method used herein. It was found that the uncertainty in the strain measurements is of the order of 100 micro-strains or 0.01%.

The Cartesian-based strain contour maps were mapped to a cylindrical polar coordinate system via the following transformation

$$\begin{bmatrix} \varepsilon_{rr} & \varepsilon_{r\theta} \\ \varepsilon_{\theta r} & \varepsilon_{\theta\theta} \end{bmatrix} = R^T \begin{bmatrix} \varepsilon_{XX} & \varepsilon_{XY} \\ \varepsilon_{YX} & \varepsilon_{YY} \end{bmatrix} R \qquad (1a)$$

where $\varepsilon_{r\theta}=\varepsilon_{\theta r}$, $\varepsilon_{XY}=\varepsilon_{YX}$, and the rotation tensor $R$ is

$$R = \begin{bmatrix} \cos \theta & -\sin \theta \\ \sin \theta & \cos \theta \end{bmatrix} \qquad (1b)$$

Note that the computation of the angles in the polar coordinate system first requires the selection of its origin. This system (wherein $r$ and $\theta$ are position coordinates relative to Cartesian $X$ and $Y$ coordinates), is shown schematically in Fig. 3, and was chosen to be at that point in each digital grid (shown on the PFSA membrane image in the figure) located within 2 pixels of the coupon center.

**2.7 Experimental Procedure.** Prior to immersion, several digital images of each coupon (with contrast features facing the camera lens) were captured to serve as reference images. The drum/coupon assembly was then immersed (on edge) into a bath of $80\,°C$ water for 5 min. Following extraction, residual water remaining on the assembly was allowed to drain back into the bath for 5 s. The assembly was the placed beneath the camera (see Fig. 2) and the image recording process continued. The initial location of the drum assembly (prior to immersion) was recorded with scribe marks on the mounting base so as to preclude significant errors from rigid body translation/rotations and to minimize lost image data relative to the initial field of view (small rigid body translations/rotations do not affect strains predicted with the DIC method). The total drying time for each test was arbitrarily selected at 26 h (longer drying times revealed no significant changes in the accumulated in-plane strains in either material).

The Cartesian DIC grid patterns consisted of 1776 grid points, with 48 grid points along the horizontal direction and 37 grid points along the vertical direction. This grid pattern, which covered a rectangular area of $\sim$1500 mm$^2$ (based upon an estimate of a $2X$ system magnification for the images analyzed with the DIC algorithm), was used only for the cumulative DIC analyses.

## 3 Results and Discussion

The cumulative and incremental strain fields measured in three PFSA membrane (i.e., D1, D2, D3) and three MEA (i.e., T1, T2, T3) tests are discussed in detail. Numerous additional coupons were tested (with image capture rates comparable to those used in the reported tests) only to reveal very similar strain evolution and strain maps for the in-plane strain components (all $E_{rr}^{\text{dried}}$ and $(E_{rr}+E_{tt})^{\text{dried}}$ values not reported herein fall within the range of values reported in Table 1).

**3.1 Mechanical Strain Evolution During Drying.** Before discussing the DIC results, it is useful to summarize the anticipated deformation behavior since this will aid in the interpretation of the DIC results [2,10]. As mentioned above, the membrane shrinks by up to 8% during a hydration/dehydration cycle. If a perfectly uniform drying state exists in the material, then one would expect to see a null strain contour plot (i.e., no discernable point-by-point variation in strain) even though significant tension may be induced from shrinkage. This is analogous (for example) to the uniform cooling of a steel bar fixed at both ends, where the mechanical strain $\varepsilon_M$ is related to the total stress $\sigma$ and the modulus of elasticity $E$, via

$$\varepsilon_M = E\sigma \qquad (2a)$$

The total strain $\varepsilon$, is given by

**Table 1 Selected strain field values at $r=0$, $\theta=0$ deg (the coupon center) and $r=25$ mm, $\theta=180$ deg (a point 50 pixels from the constrained edge following the coordinate system in Fig. 3) for the PFSA membrane tests (D1–D3) and the MEA tests (T1–T3). $E_{rr}^{\mathrm{dried}}$, $(E_{rr}+E_{tt})^{\mathrm{dried}}$ refer to the radial strain and sum of radial and hoop strains at 26 h of drying**

| Test | Position | $E_{rr}^{\mathrm{dried}}$ (%) | $(E_{rr}+E_{tt})^{\mathrm{dried}}$ (%) |
|------|----------|------|------|
| D1 | $r=0$ mm, $\theta=0$ deg | 3.98 | 10.70 |
| D2 | $r=0$ mm, $\theta=0$ deg | 5.51 | 10.20 |
| D3 | $r=0$ mm, $\theta=0$ deg | 5.70 | 10.40 |
| D1 | $r=25$ mm, $\theta=180$ deg | −5.17 | −5.03 |
| D2 | $r=25$ mm, $\theta=180$ deg | −3.27 | −0.41 |
| D3 | $r=25$ mm, $\theta=180$ deg | −6.09 | −4.84 |
| T1 | $r=0$ mm, $\theta=0$ deg | 1.08 | 4.14 |
| T2 | $r=0$ mm, $\theta=0$ deg | 0.29 | 1.77 |
| T3 | $r=0$ mm, $\theta=0$ deg | 1.25 | 3.43 |
| T1 | $r=25$ mm, $\theta=180$ deg | −2.66 | −1.35 |
| T2 | $r=25$ mm, $\theta=180$ deg | −0.62 | −0.62 |
| T3 | $r=25$ mm, $\theta=180$ deg | −2.52 | −1.33 |

$$\varepsilon = \varepsilon_M + \varepsilon_{\mathrm{Th}} \qquad (2b)$$

where $\varepsilon_{\mathrm{Th}}$ is the thermal strain. If both ends of the bar were fixed, the measurable total strain $\varepsilon$ would be zero and $\varepsilon_M = -\varepsilon_{\mathrm{Th}}$. Therefore, the steel bar would not have measurable total strain (using the DIC technique, for example) but it would have mechanical stress and mechanical strain. Due to the viscoelastic behavior of PFSA membranes (and MEAs), Eq. (2b) is rewritten as

$$\varepsilon(X,t) = \varepsilon_M(X,t) + \varepsilon_{\mathrm{HT}} \qquad (3a)$$

where

$$\varepsilon_M(X,t) = \int_{-\infty}^{t} J(X, t-\tau) \frac{\partial \sigma(X,\tau)}{\partial \tau} d\tau \qquad (3b)$$

and $X$ is an arbitrary (in-plane) position coordinate, $t$ is time, $J$ is the creep compliance, and $\varepsilon_{\mathrm{HT}}$ is hygro-thermal strain [2]. Note that the sign convention in Eqs. (2) and (3) is such that tensile strain (or swelling) is positive and compression (or shrinkage) strain is negative. The origin of shrink tension in the membrane is as follows. In a fully constrained membrane undergoing uniform drying, there will be no measurable total deformation (i.e., $\varepsilon(X,t)=0$), and the shrinkage (denoted by $\varepsilon_{\mathrm{HT}}$, a negative value) would induce a positive mechanical strain since $\varepsilon_M(X,t)=-\varepsilon_{\mathrm{HT}}$, and the stress $\sigma$ in Eq. (3b) will be positive: hence the term shrink tension is applied in this situation. In the case of nonuniform drying, there will be regions of the material that are dryer than adjacent regions. The dryer regions will develop shrink tension first, which in turn causes them to "pull" on the wetter (and therefore much more viscoelastically compliant) regions. The result is that in either local region $\varepsilon_M(X,t) \neq -\varepsilon_{\mathrm{HT}}$ and $\varepsilon(X,t) \neq 0$. Therefore, the resulting DIC strain contours would suggest nonuniform strain evolution during drying. In the dryer regions, $\varepsilon_M(X,t) < -\varepsilon_{\mathrm{HT}}$ and $\varepsilon(X,t) < 0$ (i.e., the strain in the 2D contour plot is negative). In the wetter regions, $\varepsilon_M(X,t) > -\varepsilon_{\mathrm{HT}}$ and $\varepsilon(X,t) > 0$ (i.e., the strain in the 2D contour plot is positive). Although we cannot directly measure the mechanical strain, $\varepsilon_M(X,t)$, which is related to the existing tensile stress field and ultimately to mechanical failure of the material, we can estimate the mechanical strain by the sum of the DIC-measured total strain $\varepsilon(X,t)$ and the membrane shrinkage ($-\varepsilon_{\mathrm{HT}}$ in Eq. (3a)). For example, with a constant 8% shrinkage (i.e., $\varepsilon_{\mathrm{HT}}=-8\%$) in the membrane, a 6% total strain (i.e., $\varepsilon(X,t)=6\%$) would suggest that the mechanical strain $\varepsilon_M(X,t)=\varepsilon(X,t)-\varepsilon_{\mathrm{HT}}$ is 14% (note that the mechanical strain is composed mostly of viscoelastic creep strain and some elastic strain). Once the mechanical strain is known, the evolution of the

stress field due to shrink tension (which is assumed to be the sum of elastic and viscoelastic components) can be computed via Eq. (3b).

**3.2 PFSA Membrane Tests.** Figure 4 shows selected digital images recorded during test D1. Figure 4(a) is the as-mounted membrane surface with the black ink dot contrast pattern prior to immersion (same image as that in Fig. 3(b) but without the digital grid and coordinate system schematic). With the camera and image acquisition software activated, the drum/coupon assembly was removed from its position in Fig. 2 and immersed in hot water. After extraction, it was repositioned beneath the camera in its original location. The image capture rate was initially one image every 10 s for 45 min., giving a total of 251 images (including those for which no data was recorded during the immersion process. The image capture rate was reset to one image every 30 min of drying for 15 h. A final image was captured at 26 h leaving the total number of images captured for test D1 at 284.

Immediately after extraction, the membrane adopted a "bowl" shape with its center point depressed well below its edges. Each coupon followed this geometry after extraction from the hot water bath. In addition, a crease also developed as shown in Fig. 4(b), which is an image of the membrane after 1.8 min of drying. Note that the crease is a distortion of the initial contrast pattern that would preclude use of Fig. 4(b) in the DIC analysis. Even though every attempt was made to remove residual water, water "bands" (i.e., light regions) appeared along the image periphery in Fig. 4(b) and ran perpendicular to the circumference of the bowl-shaped geometry. Figures 4(c) and 4(d) are digital images of the membrane surface after 3.5 and 12 min drying periods, respectively. Note that each image shows decreased amounts of residual water (lighter regions), with less water apparent in Fig. 4(d) than in Fig. 4(c). The membrane was essentially planar (i.e., the bowl-shape vanished) in Fig. 4(c). Figures 4(c) and 4(d) also show that the crease in Fig. 4(b) vanished during drying. For the cumulative DIC analysis, the image in Fig. 4(e) was compared with the image in Fig. 4(f) captured when the 26 h drying period terminated. These images are shown with the representative $\sim 1500$ mm$^2$ digital grid pattern (periodic array of dots) superimposed by the DIC algorithm.

Since we were primarily interested in the drying-induced strain fields at long drying times, images were gathered at 30 min intervals in tests D2 and D3. Again, strain fields in the membranes were computed via DIC analysis on the initial image and that following the 26 h drying period. There was no obvious difference between the digital images recorded in tests D2 and D3 (the bowl-shaped geometry in both cases vanished after 3.5 min of drying with no lingering defects) and Figs. 4(e) and 4(f), are appropriate representations of those gathered in these latter two tests. Additional tests (not reported) on PFSA coupons revealed the same behavior.

Figures 5(a)–5(c) show cumulative contour maps (covering 1500 mm$^2$ of coupon surface area) of the radial ($\varepsilon_{rr}$), hoop ($\varepsilon_{\theta\theta}$) and, shear strain ($\varepsilon_{r\theta}$) fields, respectively, computed via the cumulative DIC method and Eq. (1). Values of the strain contours at a given point and time are, respectively, denoted by $E_{rr}, E_{tt}$, and $E_{rt}$ in the map keys. This involved correlation of the initial (Fig. 4(e)) and final (Fig. 4(f)) images in test D1 (i.e., comparison of dry states only). The filled white circle at the center of each map denotes the origin of the polar coordinate system in Fig. 3. Figure 5(a) shows a maximum (tensile) radial strain of 6.2% about the membrane center, whereas the greatest compressive strain of −6.7% accumulated along the periphery (or regions closest to the constrained edge). This suggests that the membrane dried more quickly along its periphery which is not surprising in light of the thermal mass of the drum fixture. Shrink tension therefore initially developed along the membrane periphery causing tension in the remaining portion of the membrane. As this tension increased, strains near the periphery relaxed and became compressive: this
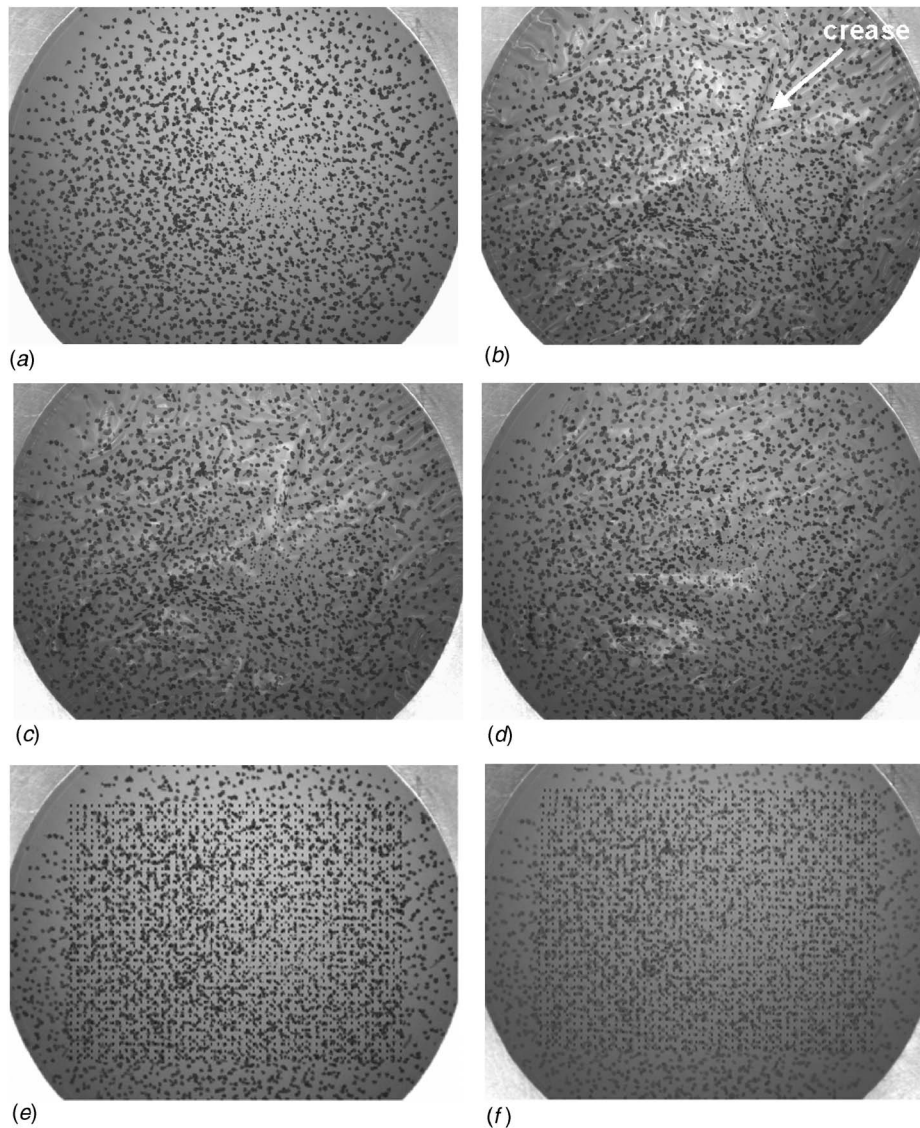
**Fig. 4 Digital images of PFSA membrane surface (mounted in the drum fixture) with contrast pattern in test D1: (*a*) prior to immersion; (*b*) with crease after 1.8 min drying; (*c*) after 3.5 min drying; (*d*) after 12 min drying; (*e*) digital grid (periodic black dots) on image in (*a*); (*f*) digital grid on final image recorded at the end of drying (26 h). Maximum radial field of view is 28.5 mm.**

follows our previous observation that $\varepsilon < 0$ in drier portions of the membrane. Before the inner region of the membrane dried out, it was under continual creep deformation. When fully dried, shrink tension developed, and the inner region came into force equilibrium with its periphery. When equilibrium was achieved, the strain field in the membrane was "frozen-in" and displayed in all cumulative strain contour plots. Although no cycled hydration/dehydration tests were attempted, it is conceivable that when the coupon is under repeated hydration/dehydration cycles with the outer circumference drying out faster, the mechanical strain in the inner region of the coupon may increase. Based upon this observation, we surmise that creep rupture, as a result of strain accumulation from the repeated hydration/dehydration cycles, may be one of the mechanical failure mechanisms in polymer electrolyte membranes. It should be noted that this mechanism is different from that due to stress-control fatigue failure proposed in [2]. Unfortunately, neither mechanism has been conclusively demonstrated from in-situ fuel cell testing. This is due in part to complications resulting from interactions between chemical degradation

and mechanical stress. Another reason is that most fuel cell durability tests are conducted far beyond the onset point of mechanical failure and this makes identification of the failure mechanism problematic.

Figure 5(*b*) shows a peak hoop strain of 6.7% corresponding to the two dark contour lobes positioned about the membrane center. The minimum hoop strain of −3.1% appears in contours along the membrane periphery. Note that the peak hoop strain contour lobes fall in between the dark lobes in the radial strain contours in Fig. 5(*a*). For example, the radial strain contours suggest that the membrane is "stretched" in the radial direction along an axis perpendicular (and running through) the center of the peak strain lobes. Alternatively, peak hoop strains develop in the peripheral contour lobes in Fig. 5(*b*) that are positioned at an angle relative to the peak radial strain contours in Fig. 5(*a*). This suggests that even though the periphery of the membrane dried out quicker, it did not dry uniformly. Otherwise, the contour plots would consist solely of concentric rings. Figure 5(*c*) shows contours of the shear strain
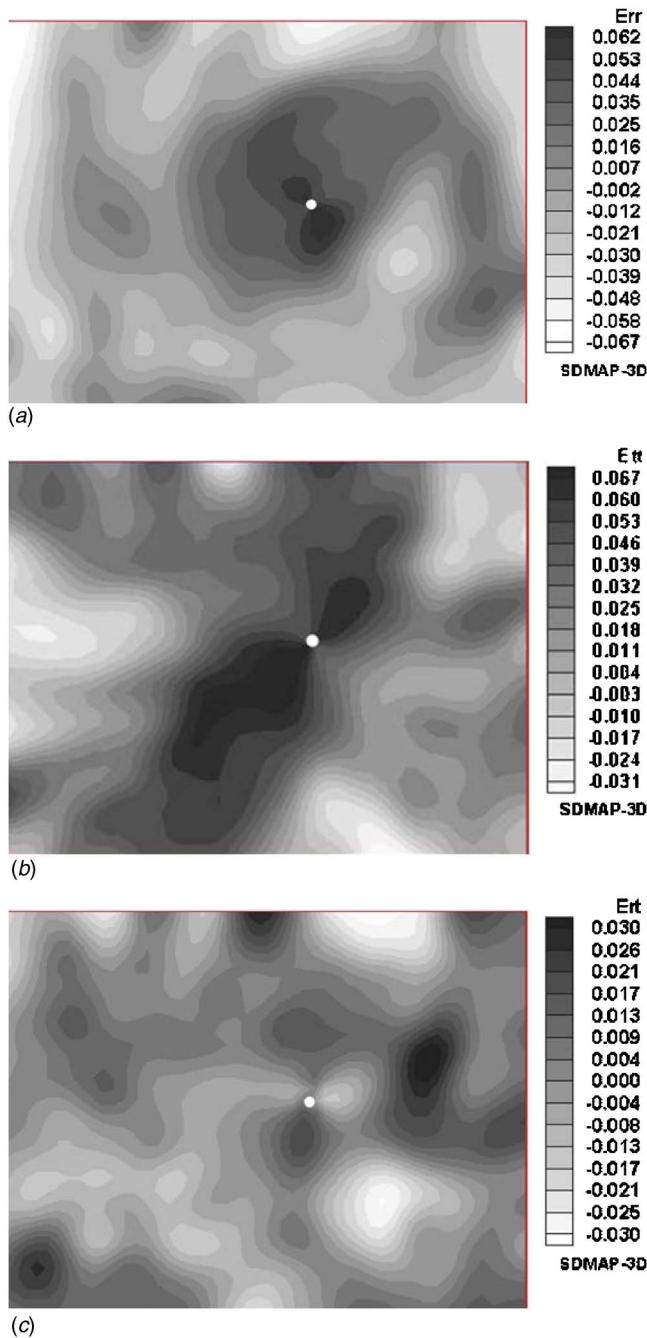
(a)



(b)



(c)

**Fig. 5 Cumulative strain maps from correlation of initial and final PFSA membrane digital images in test D1 (see Figs. 4(e) and 4(f)) over a 26 h drying time: (a) contours ($E_{rr}$) of radial strain $\varepsilon_{rr}$; (b) contours ($E_{tt}$) of hoop strain $\varepsilon_{\theta\theta}$; (c) contours ($E_{rt}$) of shear strain $\varepsilon_{r\theta}$. The filled white circle (superimposed) in each image represents the origin of the polar coordinate system (see Fig. 3) for strain measurement.**

distribution after the 26 h drying time. Note that cumulative radial and hoop strain patterns generated for tests D2 and D3 showed qualitative similarities to those in Fig. 5.

Due to conservation of mass (and to a lesser extent volume), one would expect a thickness variation from the membrane periphery to its center. No attempt was made to link thickness variations with the strain maps since the latter were generated purely from surface data. Based upon previous experience with ex situ weight measurements, we did not expect significant weight change before and after each DIC test. Therefore, no weight

change measurements were attempted.

Although we did not rigorously quantify the water concentration and temperature at various locations in each hydrated coupon, we estimated that the peripheral regions dried out earlier than regions close to the membrane center by about 20 min. Using the thermal diffusivity of the PFSA membrane material ($5 \times 10^{-5}$ cm$^2$/s, estimated as 40% of liquid water thermal diffusivity for a wet membrane with 40% water content [1]), it is estimated that an 18-$\mu$m-thick membrane cools from $80\,^{\circ}$C to $25\,^{\circ}$C in less than 0.1 s (i.e., for material at or proximate to the membrane center). However, the time to reach the peak strain is not determined by the cooling rate, but rather, by how fast the membrane dries out from an over-saturated condition to ambient RH. We therefore measured the temperature of the membrane at the drum fixture rim using a thermocouple placed between the membrane and one of the steel ribs of the drum fixture. Over a period of 10 min the drum fixture cooled to $60\,^{\circ}$C. We conclude that the membrane edge dried in about 10 min, which is substantially shorter that what we estimate is a 30–40 min drying time for the membrane center. Beyond 30–40 min, the shrink tension in the membrane periphery will come into equilibrium with regions surrounding the membrane center, and the strain field in the membrane stops changing.

Figures 6(a)–6(d) show the evolution of the radial strain contour $E_{rr}$ and the sum of the radial and hoop strain contour values $E_{rr}+E_{tt}$, at $r=0$, $\theta=0$ deg (i.e., the membrane center, see Fig. 3) and $r=25$ mm, $\theta=180$ deg (a point at the membrane periphery approximately 50 pixels from the inner edge of the drum relative to the coordinate system in Fig. 3) for tests D1 and D3. The variation of strain contour values is shown for the first 1.4 h of drying time. The data for each plot was generated via incremental correlation of temporally successive images at the grid points sitting at the center of $30 \times 30$ pixel arrays. The initial image was chosen to be the dry membrane at the outset of the test. Incremental correlation was then run backwards in time so as to compare the dry state with different stages of drying (i.e., initially dry-dry, then dry-hydrated, then hydrated-hydrated). In Fig. 6(a), the upper and lower curves suggest that the radial strain is tensile at $r=0$, $\theta=0$ deg and compressive at $r=25$ mm, $\theta=180$ deg, respectively. At the center point, the radial strain increases after the start of the test and peaks at 9.5%, 0.10 h. Beyond this time, it decreases until a constant strain of 3.98% is attained around 0.5 h. Substantially less change with time occurs at $r=25$ mm, $\theta=180$ deg with a peak strain of $-6.79$% changing to a constant strain of $-5.17$% achieved after 0.5 h. Figure 6(b) shows that $|E_{rr}+E_{tt}| > |E_{rr}|$ at $r=0$, $\theta=0$ deg for the duration of the test. The behavior depicted in Figs. 6(a) and 6(b) for $t<0.5$ h is typical of viscoelastic polymeric materials and is in qualitative accord with [2]. Alternatively, the earliest drying stages of tests D2 and D3 showed a continuous decrease in radial strain at $r=0,\theta=0$ deg and an essentially constant compressive strain at $r=25$ mm, $\theta=180$ deg, as shown in Figs. 6(c) and 6(d) for test D3. This behavior resulted from the protracted image sampling rate (0.5 h), which precluded capture of the rise and fall of strain at the early stages of drying. Table 1 summarizes the strain values measured at 26 h of drying time for each of the six tests at $r=0$, $\theta=0$ deg and $r=25$ mm, $\theta=180$ deg. Differences in the drying strains are due in part to small quantities of water remaining on each membrane surface following extraction from the hot water bath, and subsequent nonuniformity of drying across each coupon surface.

**3.3 MEA Tests: Top Illumination.** The geometry of the MEA coupons following extraction from the hot water bath resembled the bowl-shaped configuration of the immersed PFSA membrane, although no local defects in the MEA geometry, such as the crease in Fig. 4(b), were noted in any of the MEA coupons tested. As was the case with the PFSA coupons, the MEA coupons dried to a planar configuration with no wrinkles.

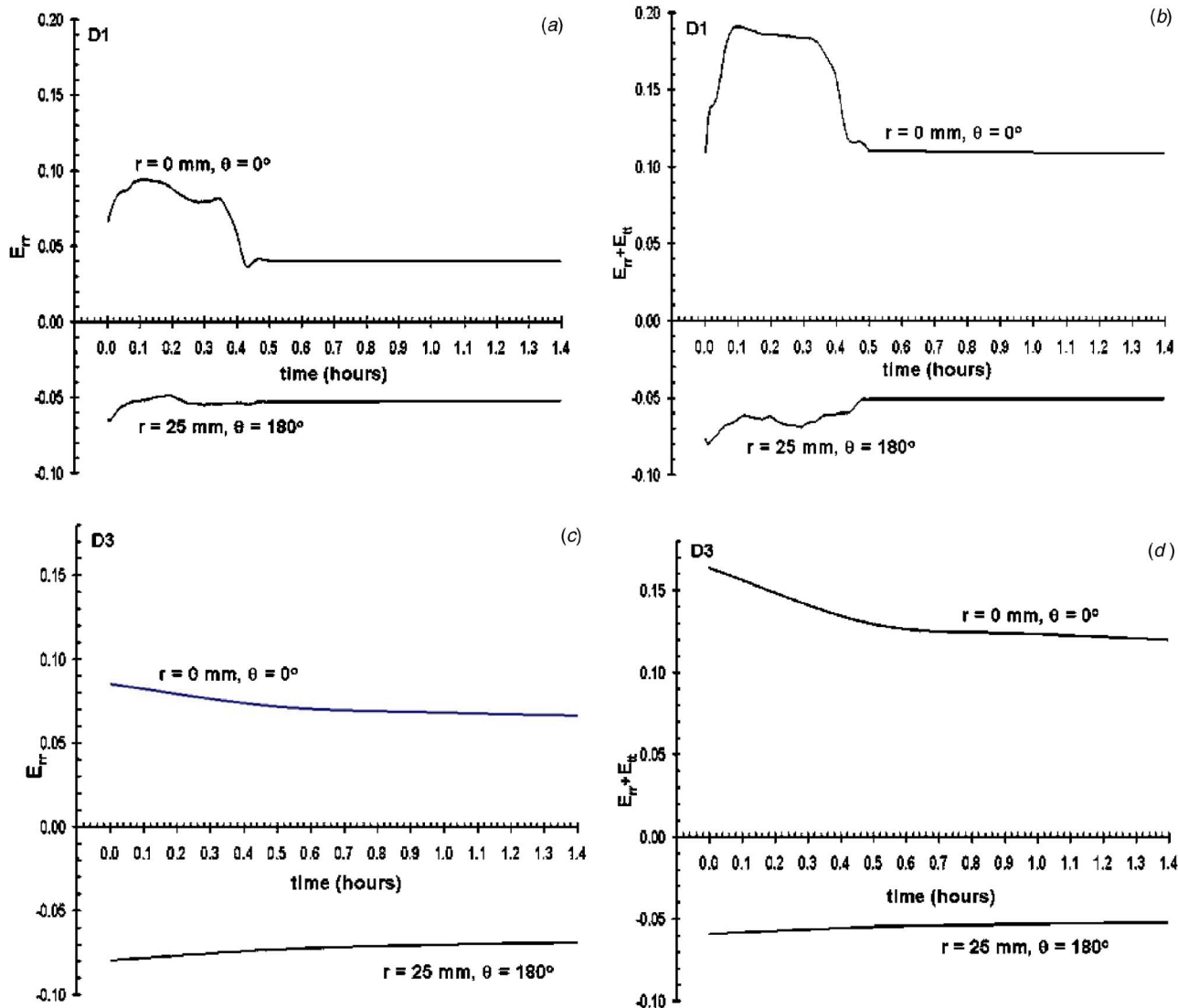Cumulative correlation of images from the drying MEA cou-

**Fig. 6  Evolution of true strain at the membrane center ($r=0$, $\theta=0$ deg) and a peripheral point ($r=20$ mm, $\theta=180$ deg) over first 1.4 h of drying (from incremental analysis). Strain contour values represented by $E_{rr}$ and $E_{tt}$, respectively, following the strain map keys in Fig. 5. (a) radial strain contours $E_{rr}$ from D1; (b) shear strain contours $E_{tt}$ from D1; (c) radial strain contours $E_{rr}$ from D3; (d) hoop strain contours $E_{tt}$ from D3.**

pons required application of the white dot contrast pattern shown in Fig. 7, which is a digital image of the MEA T1 surface prior to hot water immersion. Care was taken in the course of applying the white contrast features to each MEA surface so as not to overlap adjacent dots and hence ensure a suitable distribution of unique contrast features.

Cumulative strain contours in cylindrical polar coordinates resulting from DIC analysis of images gathered during drying of MEA test T1 are shown in Figs. 8(a)–8(c). Comparison of extrema in the radial and hoop strains in Figs. 8(a) and 8(b) with those in the Figs. 5(a) and 5(b) show that the MEA material accumulated less strain at the longest drying time than the PFSA material. For example, the peak radial strain in Fig. 8(a) is 2.7% after 26 h, whereas that in the PFSA membrane in Fig. 5(a) is 6.2%. Similar observations apply for the hoop and shear strain distributions in MEA T1. This suggests that the electrode layers provide stiffening to the membrane and reduce creep strain. Note that the distributions of extreme strain values in Figs. 8(a)–8(c) (as denoted by the irregular contour geometries) are far less uniform than those for the membranes. For example, the peak radial strains in Fig. 8(a) are concentrated in lobes that are nonuniformly



**Fig. 7  Digital image of MEA coupon T1 (with white dot contrast pattern) in drum fixture. Note that portions of the digital grid superimposed on the coupon image appear as small black dots on the white dots.**
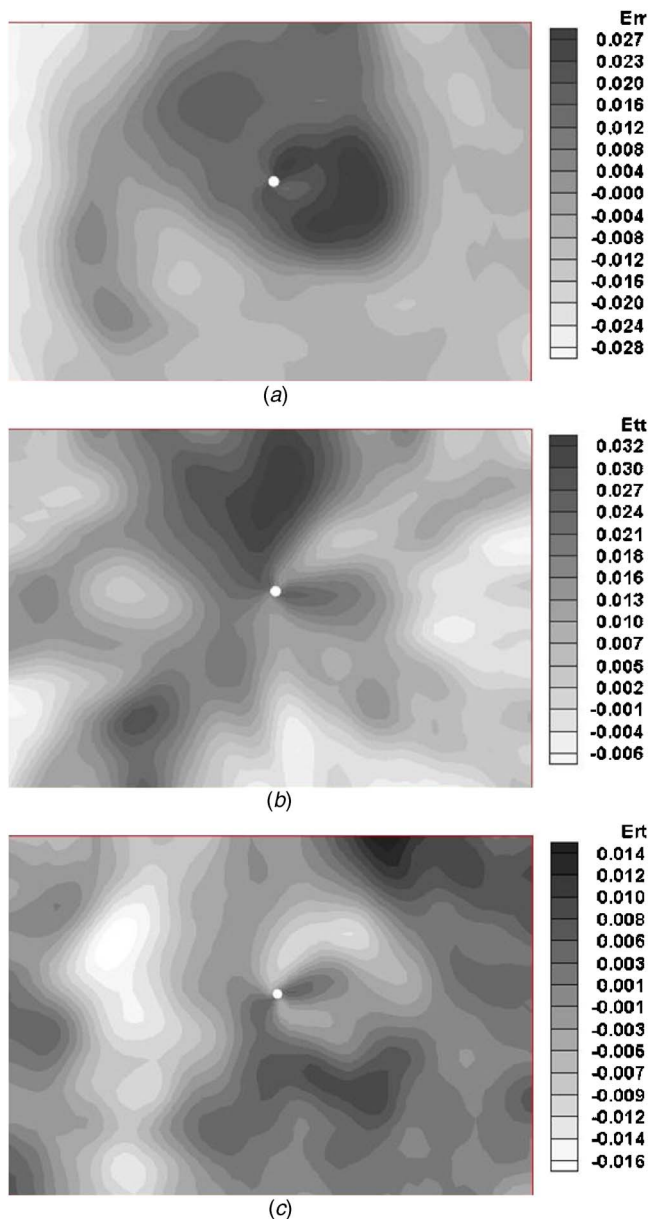
Err
0.027
0.023
0.020
0.016
0.012
0.008
0.004
-0.000
-0.004
-0.008
-0.012
-0.016
-0.020
-0.024
-0.028

(a)

Ett
0.032
0.030
0.027
0.024
0.021
0.018
0.016
0.013
0.010
0.007
0.005
0.002
-0.001
-0.004
-0.006

(b)

Ert
0.014
0.012
0.010
0.008
0.006
0.003
0.001
-0.001
-0.003
-0.006
-0.007
-0.009
-0.012
-0.014
-0.016

(c)

**Fig. 8 Cumulative strain maps comparing initial and final digital images from MEA test T1 over a 26 h drying period. (a) contours ($E_{rr}$) of radial strain $\varepsilon_{rr}$; (b) contours ($E_{tt}$) of hoop strain $\varepsilon_{\theta\theta}$; (c) contours ($E_{rt}$) of shear strain $\varepsilon_{r\theta}$. The filled white circle (superimposed) in each image represents the origin of the polar coordinate system (see Fig. 3) for strain measurement.**

positioned about the MEA coupon center. A large (dark) lobe of extreme tensile radial strains surrounds a much smaller (gray) contour lobe of lower tensile strains. Compressive radial strains tend to accumulate along one edge of the MEA strain contour map, as indicated by the lighter-shade contour patch at the left (similar contours were noted along the edges of maps from additional MEA samples tested with different digital grid patterns). It is interesting to note that the dark contour lobe projecting upwards of center in Fig. 8(b) represents a region of peak hoop strain that is not mirrored by a comparable patch downwards of center (cf. Fig. 5(b)). This distribution of hoop strain suggests that one of the principal strains is greater than the other, and hence the stress field deviates from a balanced bi-axial state. In the shear strain field plot in Fig. 8(c), lobes of strain extrema are primarily downwards of center. Note that similar observations were made from the cu-

mulative strain contour maps of MEA tests T2 and T3.

Figures 9(a)–9(d) show the evolution of the $E_{rr}$ and $E_{rr}+E_{tt}$ strain contour values in the MEA coupons at $r=0$, $\theta=0$ deg and $r=25$ mm, $\theta=180$ deg. The images for T1 were gathered in the same fashion as those for D1. Qualitative comparison of Figs. 9(a) and 9(b) with Figs. 5(a) and 5(b) shows essentially the same viscoelastic behavior for the two materials. Perhaps the most significant difference between the strain evolution results of tests D1 and T1 is the peak radial strain values (see Table 1). Similar behavior is noted in Fig. 9(b), which shows the evolution of $E_{rr}+E_{tt}$. The results shown in Figs. 9(c) and 9(d) resemble those of D3 in Figs. 5(c) and 5(d) involving the 30 min image sampling rate. The carbonaceous layer on the MEA leads to lower strain levels and less uniform strain fields than those in the PFSA membrane material. The rate at which the strain changed in the MEA is slightly lower than that for the PFSA membrane.

**3.4 MEA Test: Bottom Illumination.** Mud cracks in the MEA are not normally visible; however, when two mud cracks from either side of the MEA cross each other, light can pass through the resulting point(s) of intersection. Since there are many intersections of mud cracks on either side, one typically sees a "stars-at-night" pattern, which may be correlated to the density of mud cracks in the MEA. The pre-existing "stars-at-night" pattern was thought to be a natural contrast pattern for the DIC measurements. This pattern is evident when one surface of the MEA is illuminated with the fiber optic source while observing the other surface. The mud cracks, or the "stars-at-night" patterns, appear as an array of brightly illuminated dots, as shown in Fig. 10(a), which is a digital image of an MEA surface (test B1) prior to hot water immersion. For the single bottom illumination MEA test reported herein, 538 digital images were captured over the 26 h drying period. Numerous additional tests on other MEA coupons revealed no significantly different results from those noted for B1.

Figures 10(a) and 10(b) are digital images of the MEA surface prior to hot water immersion and following the 26 h drying period, respectively. Comparison of Figs. 10(a) and 10(b) reveals additional bright spots in the latter image that appeared during drying. These represent additional (overlapping) mud cracks that opened in the MEA surface and are contrast features that were not in the reference image taken prior to immersion. A greater density of spots appear around the coupon center in Fig. 10(b) suggesting that mud crack nucleation is more common in regions that dry more slowly. To estimate the increase in the mud crack density, we used an image-processing program [18] to reduce each image to a 1-bit color depth and then examined the resulting histogram reading, which gave the number of black and white pixels. From this, we arrived at an estimated "stars-at-night" pixel count as an index of mud crack density. We found that Figs. 10(a) and 10(b) contain 0.8% and 1.8% white pixels, respectively. This suggests a 120% increase in the mud crack density after just one hydration/dehydration cycle (additional MEA tests gave densities in the 118–123% range). We consider this an important observation since it implies that the strength in the electrode layer is relatively low compared with that of the PFSA membrane alone. It is the drying-induced changes to the mud crack density that precluded analysis of strain evolution in the bottom-illumination mode: the DIC algorithm can only track the same contrast features in each image from start to finish.

## 4  Concluding Remarks

Strain accumulation during drying of PFSA membrane and MEA materials was measured with a digital image correlation technique. Strain fields resulting from cumulative analyses (in which images at initial and final drying stages were compared) were computed and displayed as contours of constant strain. The evolution of the radial strain field and the sum of the radial and hoop strain fields were measured via incremental correlation at two grids points located at the center and one edge on the coupon
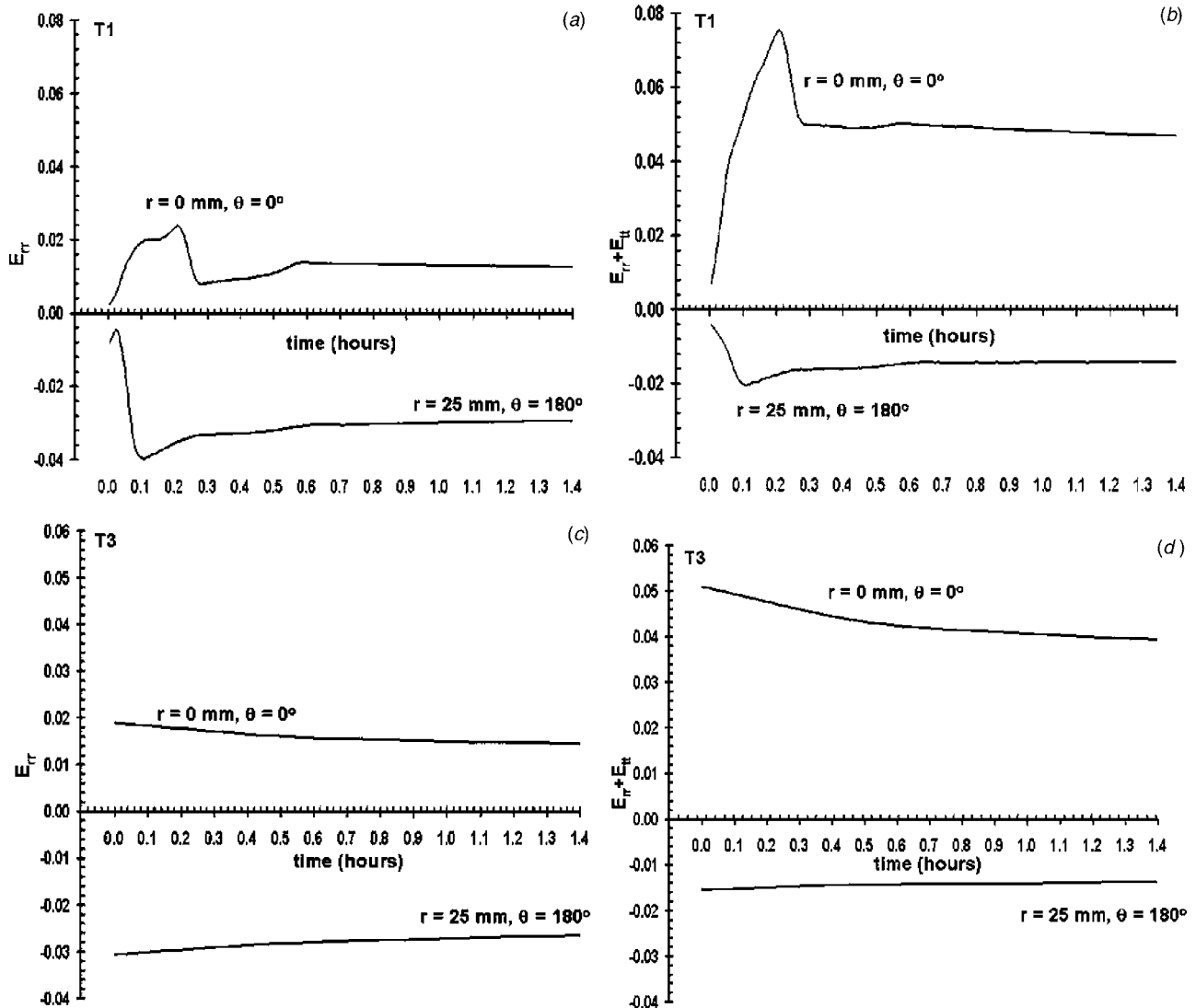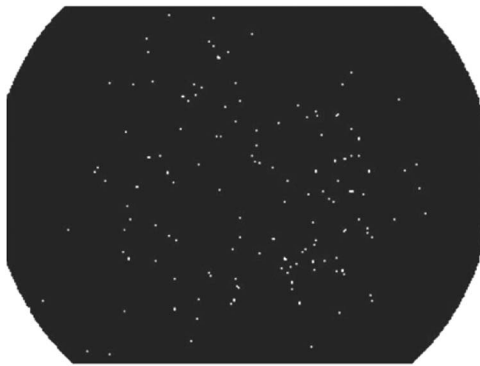
**Fig. 9  Evolution of strain at the membrane center ($r=0, \theta=0$ deg) and peripheral point ($r=20$ mm, $\theta=180$ deg) over first 1.4 h of drying (from incremental analysis). Strain contour values represented by $E_{rr}$ and $E_{tt}$, respectively, following the strain map keys in Fig. 8. (*a*) Radial strain contours $E_{rr}$ from T1; (*b*) hoop strain contours $E_{tt}$ from T1; (*c*) radial strain contours $E_{rr}$ from T3; (*d*) hoop strain contours $E_{tt}$ from T3.**

surfaces. This required correlation of temporally sequential images, beginning with those recorded before hot water immersion and ending with the last image recorded at the longest drying stages. Results from three separate tests of the PFSA membrane coupons revealed that that peak strains accumulated early in the tests; i.e., within the first 0.5 h of drying time. A slow decrease in strain followed, after which point the strains achieved constant values as drying continued. Hence, the total strain contour patterns formed during early drying stages tended to become "frozen in" at longer drying times. The distributions of radial and hoop strains suggested that peripheral regions of each coupon dried out earlier than the inner regions (due to the thermal mass of the drum fixture) and then pulled on the inner regions, creating radial strains as high as 9.5%. The observed high strains also demonstrate a strong interaction between the drying effect and the viscoelastic material properties of the membranes. Two test methodologies were explored with the MEA coupons, i.e., one that utilized a natural contrast pattern referred to as "stars-at-night" due to illumination of overlapping defects known as mud cracks in the MEA; the other used an array of white dots manually applied to one surface of each MEA coupon with an indelible marker. A significant increase (120%) of mud cracks was found in
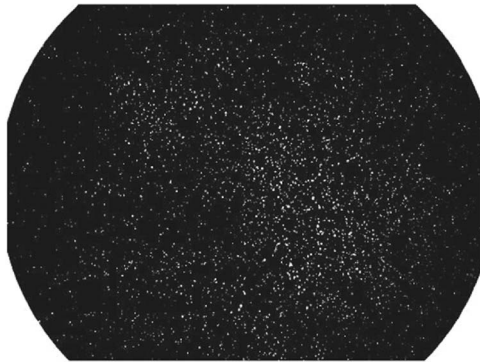
regions surrounding the coupon center which suggests that slower drying promotes mud crack nucleation in the electrode layers. Appearance of additional mud cracks during drying precluded the use of the DIC technique using the illuminated mud cracks as a contrast pattern. On the other hand, the DIC technique worked without any issues once the contrast pattern was changed to a series of white dots applied with an indelible marker. In general, strain accumulation in the MEA tends to be less uniform than that in the membrane, and corresponding peak strain values in the MEA tend to be less than those in the membrane independent of the amount of drying time, suggesting the reinforcement effect from the electrode layers lowers strain accumulation in the MEA.

**Fig. 10** Digital images of B1 MEA coupon with bottom illumination (i.e., fiber optic ring in Fig. 2 placed beneath the drum/coupon assembly): (*a*) initial field of view in dry state (i.e., prior to hot water immersion showing "stars-at-night" (white dots) pattern; (*b*) after 26 h drying time show increased density in pattern. Maximum radial field of view is 28.5 mm.

## Nomenclature

$r$ = radial coordinate
$t$ = time
DIC = digital image correlation
$E$ = Young's modulus
$E_{rr}$ = radial strain contour value
$E_{tt}$ = hoop strain contour value
$E_{rt}$ = shear strain contour value
$J$ = creep compliance
MEA = membrane electrode assembly
PEM = polymer electrolyte membrane
PFSA = perfluorosulfonic acid
ePTFE = expanded polytetrafluoroethylene
$R$ = rotation tensor
RH = relative humidity
$X$ = lateral coordinate in Cartesian system
$Y$ = transverse coordinate in Cartesian system

$\varepsilon_{HT}$ = hygrothermal strain
$\varepsilon_M$ = mechanical strain
$\varepsilon_{Th}$ = thermal strain
$\varepsilon_{XX} = \varepsilon_{XX}(X, Y, t)$ = lateral strain field in Cartesian system
$\varepsilon_{YY} = \varepsilon_{YY}(X, Y, t)$ = transverse strain field in Cartesian system
$\varepsilon_{XY} = \varepsilon_{XY}(X, Y, t)$ = shear strain field in Cartesian system
$\varepsilon_{rr} = \varepsilon_{rr}(r, \theta, t)$ = radial strain field (polar coordinates)
$\varepsilon_{\theta\theta} = \varepsilon_{\theta\theta}(r, \theta, t)$ = hoop strain field (polar coordinates)
$\varepsilon_{r\theta} = \varepsilon_{r\theta}(r, \theta, t)$ = shear strain field (polar coordinates)
$\theta$ = angular coordinate
$\sigma$ = total stress

## References

[1] Part 3: Polymer electrolyte membrane fuel cell systems (PEMFC), *Handbook of Fuel Cells—Fundamentals, Technology and Applications*, 2003, W. Vielstich, H. A. Gasteiger, and A. Lamm, eds., John Wiley and Sons, New York, Vol. 3, pp. 269–663.

[2] Lai, Y. H., Gittleman, C. S., Mittelsteadt, C. K., and Dillard, D. A., 2005, "Viscoelastic Stress Model and Mechanical Characterization of Perfluorosulfonic Acid (PFSA) Polymer Electrolyte Membranes," *Proceedings of Fuel Cell 2005: The 3rd International Conference on Fuel Cell Science, Engineering and Technology*, 23–25 May 2005, Ypsilanti, MI, ASME Paper No. 74120.

[3] Gittleman, C. S., Lai, Y. H., Lewis, C., and Miller, D. P., 2005, "Durability of Perfluorosulfonic Acid Membranes for PEM Fuel Cells," *Proceedings of the AIChE 2005 Annual Meeting*, Cincinnati, OH.

[4] Post, D., Han, B., and Ifju, P., 1994, *High Sensitivity Moiré: Experimental Analysis for Mechanics of Materials*, Springer-Verlag, New York.

[5] Steel, W. H., 1986, *Interferometry*, 2nd ed., Cambridge University Press, New York.

[6] Uan-Zo Li, J. T., 2001, "Effects of Structure, Humidity and Aging on the Mechanical Properties of Polymeric Ionomers for Fuel Cell Applications," Master's thesis, Virginia Polytechnic Institute and State University, Blacksburg, VA.

[7] http://www.dupont.com/fuelcells/pdf/extrusion_cast.pdf. DuPont, 2002, Product Information Sheets.

[8] Cleghorn, S., Kolde, J., and Liu, W., 2003, "Catalyst Coated Composite Membranes," *Handbook of Fuel Cells—Fundamentals, Technology and Applications*, W. Vielstich, H. A. Gasteiger, and A. Lamm, eds., John Wiley and Sons, Vol. 3, pp. 566–575.

[9] Laramine, J., and Andrews Dicks, A, 2003, *Fuel Cells Systems Explained*, 2nd ed., John Wiley and Sons, New York.

[10] "D882-02 Standard Test Method for Tensile Properties of Thin Plastic Sheeting," *Annual Book of ASTM Standards*, Vol. 08.01, ASTM, West Conshohocken, PA, July 2004.

[11] http://www.dasylab.net/dasylab_english/.

[12] Tong, W., 1996–2003, A User's Guide to the Yale Surface Deformation Mapping Program (SDMAP), Technical Report, Department of Mechanical Engineering, Yale University, New Haven, CT.

[13] Tong, W., Tao, H., Jiang, X., and Zhang, N., Marya, M., Hector, L. G., Jr., and Gayden, X. Q., 2005, "Deformation and Fracture of Miniature Tensile Bars With Resistance Spot Weld Microstructures: An Application of Digital Image Correlation to Dual-Phase Steels," Metall. Mater. Trans. A, **36**, pp. 2651–2669.

[14] Tong, W., Hong, T., Zhang, N., and Hector, L. G. Jr., 2005, "Time-Resolved Strain Measurements of Portevin-LeChatlier Bands in Aluminum Using A High Speed Digital Camera," Scr. Mater., **53**, pp. 87–92.

[15] Tong, W., 1997, "Detection of Plastic Deformation Patterns in a Binary Aluminum Alloy," Exp. Mech., **37**(4), pp. 452–459.

[16] Tong, W., 1998, "Strain Characterization of Propagative Deformation Bands," J. Am. Soc. Mass Spectrom., **46**(10), pp. 2087–2102.

[17] Smith, B. W., Li, X., and Tong, W., 1998, "Error Assessment for Strain Mapping by Digital Image Correlation," Exp. Tech., **22**(4), pp. 19–21.

[18] Paint Shop Pro, Version 8.10. http://www.jasc.com/.